BIOCHEMISTRY
including biophysical chemistry & molecular biology
Article

Biochemistry **2010,** *49,* 8999–9010 8999
DOI: 10.1021/bi100697d

Structure and Mechanism of the 6-Oxopurine Nucleosidase from *Trypanosoma brucei brucei*[†,‡]

An Vandemeulebroucke,[§,@] Claudia Minici,[⊥] Ilaria Bruno,[⊥] Laura Muzzolini,[⊥] Paola Tornaghi,[⊥] David W. Parkin,[∥] Wim Versées,[§] Jan Steyaert,[§] and Massimo Degano*[,⊥]

[§]*Department of Molecular and Cellular Interactions (VIB) and Structural Biology Brussels, Vrije Universiteit Brussel, 1050 Brussel, Belgium,* [∥]*Department of Chemistry, Adelphi University, Garden City, New York 11530-0701, and* [⊥]*Division of Immunology, Transplantation and Infectious Diseases, Scientific Institute San Raffaele, Milan, Italy.* [@]*Present address: Department of Biochemistry, Albert Einstein College of Medicine of Yeshiva University, Bronx, NY 10461.*

Received May 5, 2010; Revised Manuscript Received September 8, 2010

ABSTRACT: Trypanosomes are purine-auxotrophic parasites that depend upon nucleoside hydrolase (NH) activity to salvage nitrogenous bases necessary for nucleic acid and cofactor synthesis. Nonspecific and purine-specific NHs have been widely studied, yet little is known about the 6-oxopurine-specific isozymes, although they are thought to play a primary role in the catabolism of exogenously derived nucleosides. Here, we report the first functional and structural characterization of the inosine-guanosine-specific NH from *Trypanosoma brucei brucei*. The enzyme shows near diffusion-limited efficiency coupled with a clear specificity for 6-oxopurine nucleosides achieved through a catalytic selection of these substrates. Pre-steady-state kinetic analysis reveals ordered product release, and a rate-limiting structural rearrangement that is associated with the release of the product, ribose. The crystal structure of this trypanosomal NH determined to 2.5 Å resolution reveals distinctive features compared to those of both purine- and pyrimidine-specific isozymes in the framework of the conserved and versatile NH fold. Nanomolar iminoribitol-based inhibitors identified in this study represent important lead compounds for the development of novel therapeutic strategies against trypanosomal diseases.

Protozoan parasites of the *Trypanosoma* genus cause a variety of diseases, including lethal sleeping sickness (*1*, *2*). This pathology caused by *Trypanosoma brucei gambiense* or *Trypanosoma brucei rhodesiense* in humans and by *Trypanosoma brucei brucei* in livestock is endemic in Central African countries, where it has a dramatic social and economic impact. Every year, 250000−300000 people are estimated to die from lack of diagnosis and/or treatment. Chemotherapeutic intervention is currently poorly effective, because it takes advantage of the action of compounds that exhibit aspecific toxicity, such as melarsoprol, eflornithine, or suramin. It is thus clear that the development of novel, highly efficient drugs against trypanosomes represents an urgent need for a large portion of the world population (*3*).

The completion of the sequence of the *T. brucei brucei* genome reinforced hopes for the identification of new molecular targets for the design of effective drugs (*4*). The absence of nine of the ten enzymatic activities that are required to synthesize the nucleotide inosine monophosphate from simple metabolites confirmed the observation that this protozoan parasite is purine-auxotrophic. The purine bases needed for RNA, DNA, and cofactor biosynthesis are thus absorbed from the host, via the concerted actions of extracellular nucleases, phosphodiesterases, and nucleotidases (*5*). Neutral nucleosides are imported by the parasite and further processed to the purine bases via the action of *N*-glycosidases, in particular nucleoside hydrolases (NHs).[1] Trypanosomes are unique in using the NH-catalyzed reaction to this end, because prokaryotes and higher eukaryotes rely on nucleoside phosphorylases (NP) for the same process. Indeed, neither NH-like genes nor NH activity has ever been found in mammals (*6*, *7*). This dichotomy, together with the observation that more than 85% of the nucleosides taken up by trypanosomes are hydrolyzed to the free base (*8*), underscores the purine recycling pathway as an attractive target for drug design. In principle, NH activity could be inhibited by specific compounds that do not affect the activity of human NPs, hence selectively blocking this crucial parasitic pathway (*9*−*11*).

Enzymes with NH activity have been extensively characterized, from protozoa (*8*, *12*−*15*), bacteria (*16*−*19*), yeast (*20*), insects (*21*), nematodes (*19*), and archaea (*22*, *23*). NHs are classified into groups according to their specificity, including the nonspecific inosine-uridine-preferring NHs (IU-NH), the pyrimidine-specific NHs (cytidine-uridine-preferring, CU-NHs), the purine-specific NHs (inosine-adenosine-guanosine-preferring, IAG-NHs), and

[†]Supported by a grant from the Institute for the Promotion of Innovation through Science and Technology in Flanders (IWT-Vlaanderen, to A.V.), a grant from FWO-Vlaanderen (W.V.), and research grants from Cariplo Foundation and FIRB (M.D.).

[‡]Structure factors and coordinates have been deposited with the Protein Data Bank as entry 3FZ0.

*To whom correspondence should be addressed. Telephone: +39-0226437152. Fax: +39-0226434153. E-mail: degano.massimo@hsr.it.

[1]Abbreviations: NH, nucleoside hydrolase; IU-NH, inosine-uridine-preferring NH; IAG-NH, inosine-adenosine-guanosine-preferring NH; IG-NH, inosine-guanosine-preferring NH; NP, nucleoside phosphorylase; *Tbb*, *Trypanosoma brucei brucei*; *Tv* IAG-NH, NH from *Trypanosoma vivax*; *Tbb* IG-NH, IG-NH from *T. brucei brucei*; EST, expressed sequence tag; PEG-MME, polyethylene glycol monomethyl ether; pNPR, *p*-nitrophenyl β-D-ribofuranoside; 7mGuo, 7-methylguanosine; Bis-Tris, bis-(2-hydroxyethyl)aminotris(hydroxymethyl)methane; ImmH, Immucillin-H; ImmA, Immucillin-A; 8-aza-ImmH, 8-aza-Immucillin-H.

Published on Web 09/08/2010

the 6-oxopurine-specific isozymes (inosine-guanosine-preferring, IG-NHs). Three distinct NH activities have been reported in trypanosomes, namely, IU-NH (*8*), IAG-NH (*13*, *15*), and IG-NH (*24*, *25*). The structure and mechanism of IU- and IAG-NHs are well-characterized (*26*). Both isozymes distort the ribosyl moiety of the substrate to a geometry that is reminiscent of an oxocarbenium ion, via specific hydrogen bonds and interactions between the ribose hydroxyls and an active site Ca^{2+}. The nonspecific isozymes activate the leaving group nitrogenous base by protonation, and a conserved histidine residue is clearly involved in the catalytic mechanism (*7*). IAG-NHs use a combination of an intramolecular hydrogen bond in the nucleoside substrate and an aromatic stacking of the purine ring with an active site tryptophan to increase the pK_a of the base, thus allowing direct protonation of the base from the solvent (*27*). The crystal structures of both IU- and IAG-NHs from trypanosomes have aided in the design of isozyme-specific inhibitors (*11*, *15*, *28*). Nanomolar inhibitors for both isozymes are currently available, and their structures in complex with the NH enzymes can be exploited to augment their efficacy and selectivity (*28*−*30*).

The IG-NH enzymes have been isolated from *Crithidia fasciculata* (*24*) and *T. brucei brucei* (*13*) and are less well understood, from both functional and structural points of view. The kinetic parameters of this isozyme purified from *C. fasciculata* revealed that the majority of the inosine imported by the parasite from mammalian plasma would be catabolized through the IG-NH, thus making it the primary target for the design of a specific drug. The enzyme displayed an apparent trimeric quaternary structure, thus differing from both IU-NHs (tetrameric) (*31*) and IAG-NHs (dimeric) (*15*). Here we report the cloning, expression, and first in-depth enzymatic and structural characterization of the IG-NH from *T. brucei brucei* (*Tbb* IG-NH). The IG-NH differs from previously characterized NHs in amino acid composition and surprisingly shares the same quaternary structure with IU-NHs. The active site cavity is conserved in the ribosyl binding portion but differs from those of both IU- and IAG-NH isozymes in the residues involved in base discrimination. Adenosine is characterized by a low turnover number, coupled to a submicromolar K_M, hence indicating a crucial role of the 6-oxo group in catalysis. Pre-steady-state kinetic analysis of guanosine hydrolysis suggests a rate-limiting step involving the release of a ribose product. The herein reported structure−function characterization provides the missing piece in the family of trypanosomal NH enzymes, and the identification of nanomolar inhibitors of the *Tbb* IG-NH offers further opportunities for the development of a specific therapeutic approach targeting the nucleotide salvage pathway in parasites.

MATERIALS AND METHODS

Gene Identification and Cloning. The *Tbb* IG-NH enzyme was originally isolated from the parasite (*13*, *25*). Partial peptide sequences obtained from the purified enzyme were used for homology searches against the *T. brucei brucei* translated ESTs from the genome sequencing project database (not completed at the start of this study). Two distinct, partially overlapping ESTs correctly matched two IG-NH peptide sequences. These could be assembled, together with one EST containing the NH fingerprint sequence (DXDXXXDD) at the N-terminus, to a single open reading frame. Two oligonucleotides were designed on the basis of the resulting gene sequence and engineered to include the *Nde*I and *Xho*I recognition sequences at their 5′ extremities. These oligonucleotides were used in polymerase chain reactions (PCRs) on a *T. brucei brucei* genomic DNA template (strain TREU927) to amplify the *ignh* gene using the proofreading Pfu DNA polymerase. The blunt-ended PCR product was cloned in a *Sma*I-linearized pBSK(−) vector and sequenced on both DNA strands using the automated dideoxy method. The N-terminal sequence translated from the amplified gene is 100% identical to that previously reported and is distinct from that of *Tbb* IAG-NH (*13*). The cloned gene displayed four differences compared to the deposited genomic sequence (*4*), leading to two amino acid substitutions (Lys98Gln and Leu228Ser). These differences were confirmed in three independent clones obtained from different PCRs, thus suggesting either mutations in the genomic DNA used compared to the reference strain or errors in the deposited genomic sequence. Multiple-sequence alignments were created using CLUSTALW (*32*).

Protein Expression and Purification. For recombinant protein expression, the *ignh* gene was subcloned between the *Nde*I and *Xho*I sites of a pET28 vector previously digested with the same restriction enzymes. The plasmid was transformed into Rosetta(DE3) *Escherichia coli* cells for protein expression. Bacteria were grown to an OD_{600} of 0.6, and protein expression was induced by addition of 1.0 mM isopropyl β-thioglucopyranoside and incubated with shaking for either 3 h at 37 °C or 18 h at 16 °C. All the following procedures were conducted at 4 °C. Cells were harvested by centrifugation at 5000*g*, resuspended in a buffer containing 20 mM Tris (pH 8.0), 50 mM NaCl, 1 mg/mL DNase, 1 mg/mL lysozyme, and 1× Complete EDTA free protease inhibitor cocktail (Roche), incubated at 37 °C for 20 min, and disrupted by sonication. The disrupted cells were centrifuged for 45 min at 17000 rpm to separate the cell debris from the intracellular soluble fraction. The soluble phase was incubated with limiting amounts of Ni-NTA resin at 4 °C for 2 h, packed in a polypropylene column, washed extensively with binding buffer [20 mM Tris (pH 7.5), 500 mM NaCl, and 10 mM imidazole], and finally eluted with the same buffer containing 0.5 M imidazole. Elution fractions were pooled and dialyzed against a buffer composed of 20 mM Tris (pH 8.4), 150 mM NaCl, and 250 mM $CaCl_2$. The N-terminal hexahistidine tag was removed by site-specific proteolysis using thrombin at a 1:200 weight ratio, leaving a GSH tripeptide fused to the N-terminus of the recombinant enzyme. The IG-NH protein was further purified via a Superdex 200 size exclusion chromatography column with an isocratic elution in 20 mM Hepes (pH 7.4) and 300 mM NaCl. Protein was concentrated using ultrafiltration devices and stored at 4 °C. Dynamic light scattering was used to assess the ideal storage buffer that prevented nonspecific aggregation and maintained sample monodispersity. The concentration of pure protein (expressed per subunit) was determined spectrophotometrically using an ε_{280} of 52940 M^{-1} cm^{-1} (*33*). Typical enzyme preparations have a specific activity of 120 μmol min^{-1} mg^{-1} with inosine as the substrate.

Steady-State Kinetics. Initial rate kinetic measurements were taken at 35 °C in a 50 mM potassium phosphate buffer (pH 7.0). Measurements were restricted to a maximal product formation of 10% to ensure the linearity of the curves. Product formation was assessed spectrophotometrically using the difference in absorption between the nucleoside and the base. The following $\Delta\varepsilon$ values were used: −4.0 mM^{-1} cm^{-1} for guanosine at 260 nm, −1.3 mM^{-1} cm^{-1} for inosine at 250 nm, −1.4 mM^{-1} cm^{-1} for adenosine at 276 nm, −4.4 mM^{-1} cm^{-1} for 7-methylguanosine at 258 nm, 1.45 mM^{-1} cm^{-1} for purine riboside at

275 nm, −3.27 mM^{-1} cm^{-1} for ethenoadenosine at 271.5 nm, 1.5 mM^{-1} cm^{-1} for cytidine at 291 nm, −1.9 mM^{-1} cm^{-1} for uridine at 280 nm, 12 mM^{-1} cm^{-1} for *p*-nitrophenyl β-D-ribofuranoside at 400 nm, −2.29 mM^{-1} cm^{-1} for 2-aminopurine riboside at 250 nm, −1.47 mM^{-1} cm^{-1} for xanthosine at 293 nm, −1.33 mM^{-1} cm^{-1} for 5′-deoxyadenosine at 275 nm, and −1.64 mM^{-1} cm^{-1} for 3-deazaadenosine at 263 nm. The data were fitted to the Michaelis−Menten equation using Origin (Microcal). All kinetic parameters were calculated per active site, making them independent of the multimerization state of the enzyme.

Inhibition Studies. Steady-state inhibition studies were performed at 35 °C in a 50 mM phosphate buffer under saturating substrate concentrations. The apparent inhibition constants for the deoxyadenosines were determined with *p*-nitrophenyl β-D-ribofuranoside (pNPR) as a substrate at pH 7. Assays were initiated via addition of the enzyme to a solution containing a fixed amount of pNPR (5 μM) and variable concentrations of the deoxyadenosines. To determine the apparent inhibition constants for the Immucillins, inosine was used as a substrate in a coupled assay using xanthine oxidase at pH 7.5 (optimal pH of xanthine oxidase). This coupled assay has a higher sensitivity than the direct method for inosine because the hydrolysis product, hypoxanthine, is oxidized by the xanthine oxidase to uric acid, which can be monitored spectrophotometrically at 293 nm (ε_{293} of 12.9 mM^{-1} cm^{-1} for uric acid). Reactions were started via addition of the enzyme to the reaction mixture containing 500 μM inosine, 120 milliunits of xanthine oxidase/mL, and variable concentrations of inhibitor. The kinetic constants for inosine hydrolysis were determined under the same conditions to ensure the coupled assay yields kinetic parameters identical to those of the direct method. The data from the deoxyadenosine and the Immucillin inhibition experiments (8−10 data points) were fit to the Dixon linearization of the equation describing competitive inhibition:

$$v = \frac{k_{cat}[E]_0[S]}{[S] + K_M\left(1 + \frac{[I]}{K_I}\right)} \quad (1)$$

where [S] is the substrate concentration, [I] is the inhibitor concentration, $[E]_0$ is the enzyme concentration, k_{cat} and K_M are the steady-state parameters for the substrate, and K_I is the competitive inhibition constant. The use of this equation requires the assumption that the inhibitor competes with the substrate for the catalytic site (*34*). The validity of this assumption is supported by the high degree of structural similarity between the inhibitors and the substrate, and by the reported structures of nucleoside hydrolases in complex with inhibitors (*29*).

Stopped-Flow Analysis. The experimental procedures for stopped-flow analysis were described previously (*35*). Stopped-flow experiments were performed on an Applied Photophysics SX18.MV stopped-flow spectrofluorimeter. All experiments were performed at 5 °C under pseudo-first-order conditions with a minimal 4-fold excess of substrate or ligand over *Tbb* IG-NH. Multiple turnovers of substrate by *Tbb* IG-NH were followed by stopped-flow absorbance using the difference in absorption between the nucleoside and the base with the Δε values mentioned above. Changes in the *Tbb* IG-NH tryptophan fluorescence during multiple-substrate turnover and ligand binding were measured using an excitation wavelength of 280 nm and detection of emitted radiation above 305 nm, using a 305 nm cutoff filter.

Quench-Flow Analysis. Rapid-quench measurements were performed as described previously (*35*). A KinTek RQF-3 quench-flow apparatus was used. An excess of guanosine (750 μM) was mixed with enzyme (40 μM) for various reaction times and the reaction quenched with acid (0.333 M HCl). Samples were filtered at 4 °C using wetted Microcon centrifugal device micro concentrators (YM-30, regenerated cellulose, 30 kDa cutoff, Amicon). The amount of guanine was quantified using a reverse-phase C18 HPLC column (100 mm × 4.6 mm, ODS HYPERSIL RP-C18, 3 μm) attached to a WATERS HPLC system. Substrate and product were eluted with a linear gradient from 2 to 20% acetonitrile with 0.08% trifluoroacetic acid in 10 mM ammonium acetate (pH 5.0) and monitored spectrophotometrically at 260 nm.

Analysis of Pre-Steady-State Data. Linear and nonlinear curve fitting to progress curves was performed using Microcal Origin version 7. The fitting functions had the general form (eq 2)

$$y(t) = \sum_i A_i \exp(-k_i t) + vt + C \quad (2)$$

where $y(t)$ is the observed signal at time t, i is the number of transients, A_i is the amplitude of the ith transient, k_i is the observed rate constant (k_{obs}) for the ith transient, v is the steady-state velocity, and C is the offset. The fitted parameters were used to make plots of observed rate constants and amplitudes versus substrate, or ribose concentrations. The concentration dependencies of the different observed rate constants were analyzed as described previously (*35*).

The progress curves of multiple turnovers of guanosine and 7-methylguanosine (7mGuo) followed by stopped-flow absorbance were transformed to curves expressing the concentration of the base ($[B]_{obs}$) normalized for the enzyme concentration used ($[E]_0$) as a function of time and were fitted to eq 3. This equation describes a three-step mechanism with a reversible chemistry step and slower product release (Scheme 1) providing the characteristic parameters for burst kinetics: the maximal burst rate (k_{obs}), the burst amplitude (A_0), and the steady-state rate constant (k_{cat}).

$$\frac{[B]_{obs}}{[E]_0} = \frac{[E\cdot B\cdot R] + [B]}{[E]_0} = A_0[1 - \exp(k_{obs}t)] + k_{cat}t$$

with

$$k_{obs} = k_2 + k_{-2} + k_3 \quad A_0 = \frac{k_2(k_2 + k_{-2})}{(k_2 + k_{-2} + k_3)^2}$$

$$k_{cat} = \frac{k_2 k_3}{k_2 + k_3 + k_{-2}} \quad (3)$$

From the saturated values of these parameters and eq 3, the apparent rate constants of chemistry (k_2 and k_{-2}) and product release (k_3) can be determined.

Crystallization. The *Tbb* IG-NH was crystallized using the hanging drop vapor diffusion method. Equal volumes of the protein solution at 11 mg/mL and the precipitant solution consisting of 100 mM bis(2-hydroxyethyl)aminotris(hydroxymethyl)methane (Bis-Tris) (pH 6.5), 200 mM ammonium sulfate, and 22% polyethylene glycol monomethyl ether 3350 were mixed on a siliconized coverslip, inverted over a reservoir containing 0.7−1.0 mL of precipitant, and kept at a constant temperature of 18 °C. Crystals grown using IG-NH expressed at 37 °C exhibited regular, bipyramidal shapes but diffracted X-rays to barely 6.0 Å resolution and were characterized by extremely high mosaicity. Instead, the same conditions using freshly prepared IG-NH expressed at 16 °C yielded prism-shaped crystals that diffracted X-rays beyond 3.0 Å. This finding could be caused by a higher conformational heterogeneity of the protein produced at higher temperatures, because enzyme

preparations from inductions of expression at 37 °C exhibited consistently higher polydispersity (~25% vs 15%) as determined from dynamic light scattering experiments. The kinetic parameters of the enzyme, however, were not affected by the temperature of induction. Crystals were cryoprotected using a solution with the PEG-MME concentration increased to 34%, mounted on fiber loops, and plunged and maintained in liquid nitrogen for storage prior to data collection. Crystals were orthorhombic in the $C222_1$ space group, with a cell volume consistent with four IG-NH subunits in the asymmetric unit and 47% solvent content (Table 4).

Structure Determination. Data from a single crystal of unliganded IG-NH were collected on beamline ID14-EH4 of the European Synchrotron Radiation Facility (Grenoble, France) at 100 K using the oscillation method. Data were indexed, integrated, and reduced to unique reflections using XDS (*36*) to a resolution of 2.5 Å. Intensities were converted to structure factor amplitudes using TRUNCATE (*37*). Initial phases were obtained with the molecular replacement method as implemented in MOLREP (*38*) using the structure of the CU-NH YeiK monomer as a search model [Protein Data Bank (PDB) entry 1Q8F] after all ligands, solvent molecules, and ions had been removed and all nonidentical residues truncated to alanine (or glycine). Only two rotation function solutions were apparent, but all four molecules could be placed in the asymmetric unit in the partial translation function. An initial $F_o - F_c$ (ϕ_c) map calculated using data to 2.5 Å showed the expected density associated with the Ca^{2+} ion at the active site. The map, however, was heavily biased by the model phases, and substantially untraceable. The density was manually inspected, and the amino acid regions that had no electron density associated with them were removed from the model. Phases calculated to 5.0 Å resolution using the modified YeiK model were refined and extended in 1000 cycles of solvent flattening, histogram matching, and noncrystallographic symmetry averaging as implemented in DM (*39*). The molecular envelope was calculated using a 5.0 Å radius at each atom position. The final maps were of very good quality, and both the mask preparation and the number of cycles of phase refinement were crucial for the success of the procedure. The improved map allowed the tracing of all ordered regions of the IG-NH molecule. The same procedure was also successful when using the *Tv* IAG-NH or the *Cf* IU-NH as a search model for phasing, underscoring the robustness of the approach that was followed. The model was refined in cycles of manual rebuilding in electron density maps in O (*40*), and maximum likelihood energy minimization using REFMAC5 (*41*). TLS refinement was implemented in the protocol, treating each independent subunit as an individual group (*42*). MOLPROBITY (*43*) was used to validate the geometric quality of the model during the refinement. Water molecules were added at the later stages of refinement in positive peaks of $F_o - F_c$ (ϕ_c) maps greater than 3.5σ using ARP/wARP (*44*). The final residual density suggested the modeling of a Bis-Tris molecule at each active site (Figure 1 of the Supporting Information). The final crystallographic validators R_{crys} and R_{free} are 0.189 and 0.225, respectively. Residues for which no electron density was visible (the three amino acids remaining from the construct at the N-terminal end in all subunits, amino acids 227−235 in chains A, C, and D; residues 256−273 in all chains) were omitted from the model. All residues fall within the allowed regions of a Ramachandran plot.

RESULTS

Identification of the IG-NH from T. brucei brucei. The limited amino acid sequence available from the *Tbb* IG-NH was used to identify the coding gene from the partial genomic sequence available at the time of the investigation. The *Tbb ignh* gene (corresponding to entry XM_840987.1 in the *T. brucei brucei* genome) is composed of 1074 bp, encoding a protein of 357 amino acids and a calculated M_r of 39365 Da. Among the so far characterized NHs, the *Tbb* IG-NH protein displays the most similarity to the *Crithidia* IU-NH (25% identical) and *E. coli* CU-NHs YbeK/RihA and YeiK/RihB (27 and 20% identical, respectively). Unexpectedly, a significantly lower level of amino acid conservation (10%) is observed with the functionally similar *Tv* IAG-NH. The alignment of the *Tbb* IG-NH amino acid sequence with a nonspecific and purine-specific trypanosomal NH highlights the presence of two major insertions (Figure 1), corresponding to the junction between helices α8 and α9, and the loop at the C-terminal end of helix α9. While the residues mediating ribosyl binding are strictly conserved in the IG-NH, the amino acids involved in the interactions with the aglycone differ remarkably both from nonspecific and from purine-specific isozymes. Indeed, His82 and His239 of the *Crithidia* IU-NH in the *Tbb* IG-NH are substituted with Tyr and Pro, respectively. More surprisingly, both tryptophan residues that mediate the catalytic activity of the *Tv* IAG-NH are also not conserved. These differences clearly point to a different mode of substrate binding and catalytic mechanism.

Substrate Specificity. The steady-state kinetic parameters of the *Tbb* IG-NH for the common nucleosides and some nucleoside analogues are summarized in Table 1. High k_{cat}/K_M ratios were found for the majority of the common purine nucleosides, with the highest activity toward inosine and guanosine, although the value for adenosine could not be accurately determined because of the low K_M. The catalytic rate constant (k_{cat}) for inosine and guanosine hydrolysis is 2 orders of magnitude higher than that for adenosine hydrolysis, but the enzyme has a higher substrate affinity (lower K_M) for the latter. Instead, the IG-NH displays 10^3-10^4-fold lower catalytic efficiencies toward cytidine and uridine substrates, resulting from both lower turnover rates and higher K_M values. The *Tbb* IG-NH displays hallmark features of NH enzymes with respect to ribosyl moiety discrimination. Indeed, the lack of the 5′-OH group lowers the specificity constant by a factor of 5×10^4, while removal of the 2′- and 3′-OH groups abolishes turnover of deoxyadenosines. 2′-Deoxy- and 3′-deoxyadenosine do bind the enzyme with inhibition constants of 182 and 170 μM, respectively.

Inhibition of IG-NH by Immucillins. Nucleoside analogues based on an iminoribitol scaffold are well-known NH inhibitors (*9*, *10*, *45*, *46*). A selection of immucillins was screened to identify tight-binding inhibitors of *Tbb* IG-NH. Three Immucillins, Immucillin-H (ImmH), Immucillin-A (ImmA), and 8-aza-Immucillin-H (8-aza-ImmH), exhibited nanomolar apparent inhibition constants (Table 1). None of these three tight-binding inhibitors displayed slow-onset inhibition, a frequent event in binding of iminoribitol-based compounds to NHs (*29*). The highest-affinity inhibitor identified is ImmA, bearing an adenine nucleobase mimic. This finding parallels the low K_M measured for adenosine and thus underscores the fact that the 6-amino group in purines and analogues greatly enhances the affinity for the active site of *Tbb* IG-NH.

Hydrolysis of 6-Oxopurine Nucleosides by the Tbb IG-NH Follows Burst Kinetics. Multiple turnovers of guanosine hydrolysis analyzed by stopped-flow absorption spectroscopy show a very fast burst of guanine production upon mixing *Tbb* IG-NH with an excess of guanosine (Figure 2), indicating that the

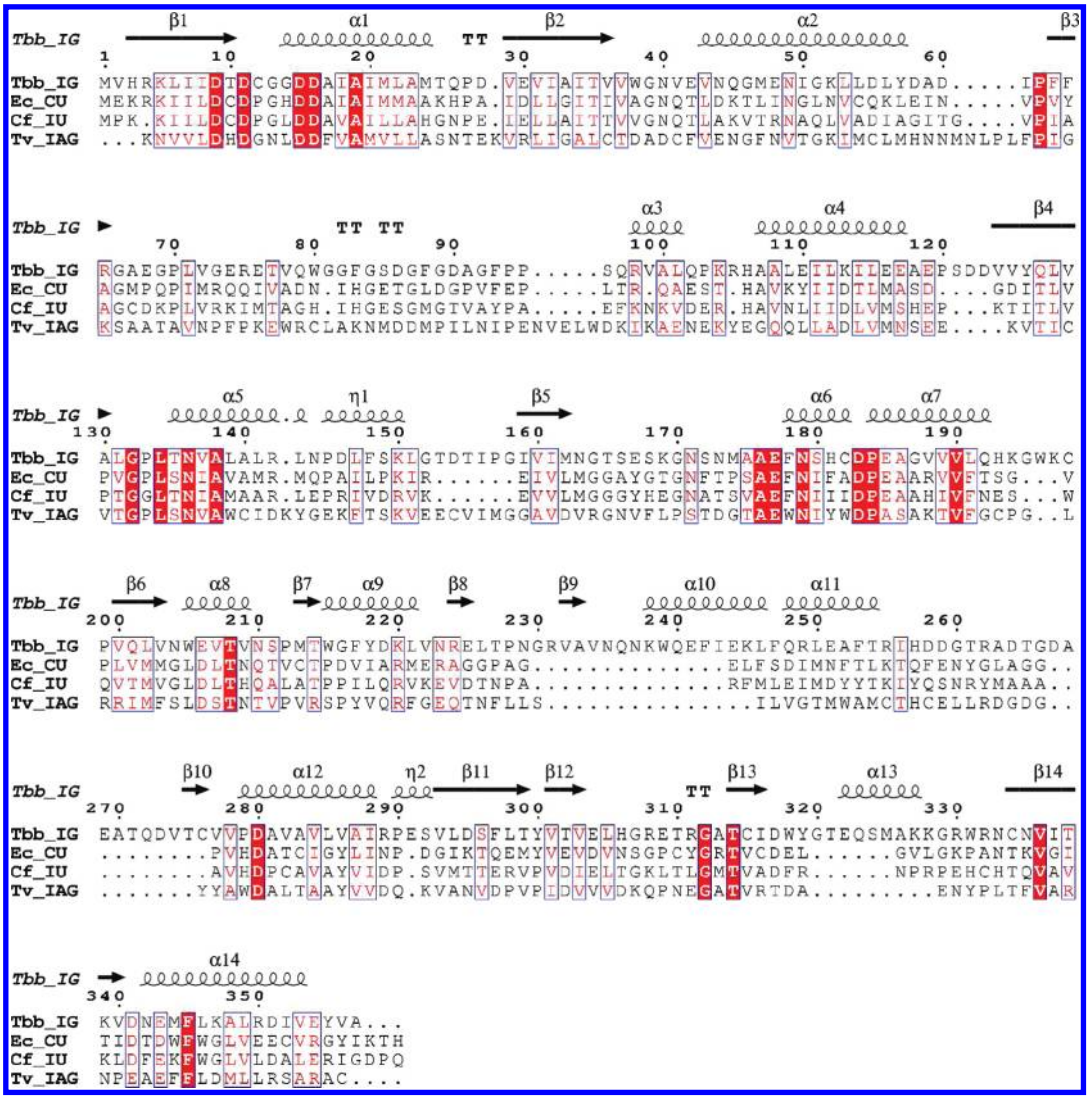

FIGURE 1: Alignment of the amino acid sequences of the *Tbb* IG-NH, the *E. coli* CU-NH YeiK (20% identical), the *C. fasciculata* IU-NH (25% identical), and the *Tv* IAG-NH (10% identical). Secondary structure elements of the *Tbb* IG-NH are depicted as arrows and ribbons at the top line of the alignment. T defines the polypeptide turn structure and η the 3_{10} helix conformation.

Table 1: Activity Profile of *Tbb*NH at pH 7 and 35 °C

substrate	k_{cat} (s^{-1})	K_M (μM)	k_{cat}/K_M (M^{-1} s^{-1})
inosine	28 ± 1	1.9 ± 0.4	(1.5 ± 0.3) × 10^7
guanosine	37.6 ± 0.5	4.5 ± 0.2	(8.3 ± 0.4) × 10^6
adenosine	0.237 ± 0.005	< 1	> 2.4 × 10^5
ethenoadenosine	6.9 ± 0.3	3.6 ± 0.7	(1.9 ± 0.4) × 10^6
cytidine	0.52 ± 0.04	271 ± 49	(1.9 ± 0.4) × 10^3
uridine	0.0038 ± 0.0008	1451 ± 600	2.6 ± 1
purine riboside	0.248 ± 0.007	0.6 ± 0.1	(3.8 ± 0.8) × 10^5
*p*NPR	0.030 ± 0.001	1.1 ± 0.3	(2.7 ± 0.6) × 10^4
2-aminopurine riboside	0.57 ± 0.02	0.8 ± 0.4	(7 ± 3) × 10^5
xanthosine	6.2 ± 0.3	280 ± 40	(2.2 ± 0.4) × 10^4
3-deazaadenosine	0.0090 ± 0.0002	2.2 ± 0.3	(4.1 ± 0.6) × 10^4
5′-deoxyadenosine	0.078 ± 0.004	240 ± 40	(3.3 ± 0.6) × 10^2

inhibitor	K_I (μM)
2′-deoxyadenosine	182 ± 50
3′-deoxyadenosine	170 ± 50
Immucillin-A	0.0044 ± 0.0009[a]
Immucillin-H	0.009 ± 0.002[a]
8-aza-Immucillin-H	0.015 ± 0.003[a]

[a]Determined at pH 7.5.

rate-limiting step occurs after hydrolysis of the N-glycosidic bond (chemistry) and thus is associated with product release. The dependence of the observed burst rate (k_{obs} in eq 3) on guanosine concentration shows saturation behavior, permitting an estimation of a maximal burst rate (the burst rate at substrate saturation) of 220 s^{-1} that corresponds to the apparent rate of chemistry. This active site titration also reveals that the maximal burst amplitude corresponds to only half of the enzyme concentration used. Multiple turnovers of the substrate analogue 7-methylguanosine (7mGuo) catalyzed by *Tbb* IG-NH also follow burst kinetics (Figure 2), showing a clear saturation behavior with a maximal burst rate of 100 s^{-1} and a maximal burst amplitude of 0.78 mol of 7-mGuo/mol of enzyme subunit.

To determine the absolute total burst amplitude, we performed a quench-flow analysis of multiple turnovers of guanosine by *Tbb* IG-NH. Guanine formation is linear as a function of time, but extrapolation of this linear guanine production back to the product axis gives a positive intercept (data not shown). This observation is a trademark for fast burst kinetics, with the burst phase occurring during the dead time of the instrument (note that the dead time of a quench-flow instrument is greater than for a stopped-flow instrument). The magnitude of the intercept equals

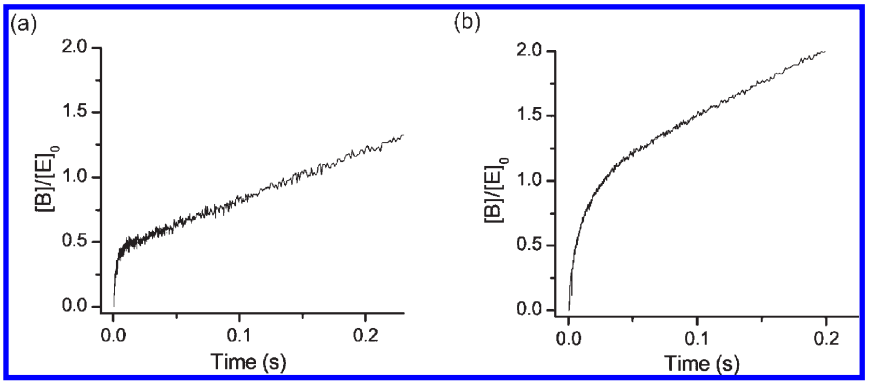

FIGURE 2: Burst kinetics of guanosine [(a) 60 μM] and 7mGuo [(b) 50 μM] turnover by *Tbb* IG-NH (5 μM) at pH 7.0 and 5 °C. The concentration of formed base [B] has been normalized for the concentration of enzyme $[E]_0$ used during the experiment; hence, the concentration of base per enzyme concentration ($[B]/[E]_0$) is plotted as a function of time.

Table 2: Parameters (k_{obs}, A_0, and k_{cat}) and Rate Constants of Burst Kinetics of Guanosine and 7-Methylguanosine Turnover by *Tbb*NH at pH 7.0 and 5 °C, Using the Nomenclature of eq 3

kinetic constant	guanosine	7-methylguanosine
k_{obs} (s^{-1})	220 ± 20	100 ± 8
A_0	0.51 ± 0.03	0.78 ± 0.01
k_{cat} (s^{-1})	1.3 ± 0.3	5.2 ± 0.2
k_2 (s^{-1})	111 ± 12	75 ± 8
k_{-2} (s^{-1})	106 ± 23	18 ± 5
k_3 (s^{-1})	2.6 ± 0.6	6.9 ± 0.4

the burst amplitude and corresponds to 0.5 mol of guanine/mol of enzyme subunit, confirming the observed burst amplitude during stopped-flow analysis. The most plausible explanation for the reduced burst amplitudes for guanosine (0.5) and 7mGuo (0.78) is a reversible chemistry step that is substrate-dependent. The progress curves of multiple turnovers of guanosine and 7mGuo catalyzed by *Tbb* IG-NH can thus be explained by a minimal three-step mechanism in which substrate binding is followed by a reversible chemistry step followed by an overall rate-limiting product release (Scheme 1).

Scheme 1: Minimal Three-Step Mechanism for the Multiple Turnovers of Guanosine and 7mGuo by *Tbb* IG-NH

$$E+S \underset{k_{-1}}{\overset{k_1}{\rightleftharpoons}} E.S \underset{k_{-2}}{\overset{k_2}{\rightleftharpoons}} E.P \xrightarrow{k_3} E+P$$

Analyzing the progress curves of multiple turnovers of guanosine and 7mGuo according to the equation describing such a three-step mechanism with a reversible chemistry step (eq 3, see Materials and Methods) allows the determination of the apparent rate constants of chemistry (k_2 and k_{-2}, the forward and reverse rate constants, respectively) and product release (k_3) as described in Materials and Methods. The apparent rates of the forward chemistry step (k_2) and product release (k_3) are very comparable for guanosine and 7mGuo hydrolysis. On the other hand, the apparent reverse rate of chemistry is almost 1 order of magnitude faster for guanosine hydrolysis than for 7mGuo hydrolysis (Table 2).

Fast Substrate Binding and Base Release. We have previously shown that multiple turnovers of purine nucleosides by *Tv* IAG-NH analyzed by stopped-flow fluorescence allow the assignment of transients to substrate binding and base release (*35*). Multiple turnovers of guanosine and inosine by *Tbb* IG-NH

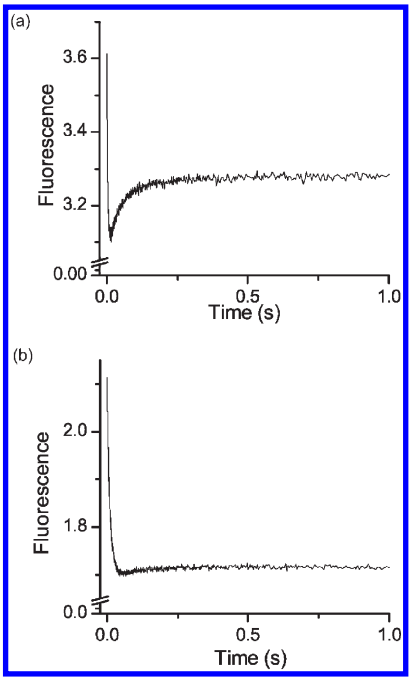

FIGURE 3: Stopped-flow fluorescence progress curves of guanosine [(a) 60 μM] and inosine [(b) 50 μM] hydrolysis by *Tbb* IG-NH (0.5 μM) at pH 7.0 and 5 °C.

also exist out of two transients (Figure 3). The first transient is characterized by a rapid and large decrease in fluorescence, while the second leads to a slower and smaller fluorescence increase. The observed rate constant of the first transient has a linear concentration dependency, which indicates that it originates from substrate binding. The rate constant of the second transient has a hyperbolic concentration dependency, representative of a transient of a process after the binding step. In analogy with the fluorescence transients observed during purine nucleoside hydrolysis by *Tv* IAG-NH (*47*), we propose that the second transient observed during hydrolysis catalyzed by *Tbb* IG-NH also involves base release. If this interpretation applies, the substrate concentration dependency of the observed rates of the transients allows us to determine the rate constants involved in substrate binding and base release (Table 3). This analysis shows that the rate of base release is 1 order of magnitude faster than the steady-state turnover rate. A fast rate of base release implies that the overall rate-limiting step must occur after the release of base.

Ordered Product Release. To determine the order of product release and validate the interpretation concerning the

Table 3: Overview of the Kinetic Constants for *Tbb*NH at pH 7 and 5 °C, Using the Nomenclature of Scheme 2

kinetic constant	guanosine	inosine	7-methylguanosine
k_1 (μM^{-1} s^{-1})	3.09 ± 0.01	2.76 ± 0.09	not determined
k_{-1} (s^{-1})	9.0 ± 0.6	4 ± 2	not determined
k_2 (s^{-1})	111 ± 12	not determined	75 ± 8
k_{-2} (s^{-1})	106 ± 23	not determined	18 ± 6
k_3 (s^{-1})	29 ± 2	6.8 ± 0.2	not determined
k_4 (s^{-1})	2.7 ± 2.5[a]	2.7 ± 2.5[a]	2.7 ± 2.5[a]
	2.6 ± 0.6[b]		6.9 ± 0.4[b]
k_{-4} (s^{-1})	270 ± 15[a]	270 ± 15[a]	270 ± 15[a]
K_D (mM)	65 ± 13[a]	65 ± 13[a]	65 ± 13[a]

[a]Rate constant determined via ribose binding stopped-flow fluorescence experiments. [b]Rate constant determined via multiple-turnover stopped-flow absorbance experiments.

fluorescence progress curves, we examined the pre-steady-state kinetics of hypoxanthine release using stopped-flow absorbance. Hypoxanthine produced during turnover of inosine by *Tbb* IG-NH was detected with a xanthine oxidase-coupled assay. At high concentrations of xanthine oxidase, a burst is apparent and the steady-state rate becomes independent of the xanthine oxidase concentration and equals the previously determined rate of steady-state turnover of inosine by *Tbb* IG-NH (data not shown). The strong absorption by xanthine oxidase prevented the observation of a saturation of the burst rate or amplitude via an increase in the xanthine oxidase concentration. It is thus not possible to determine both the rate of base release and the active site concentration from these progress curves. Nevertheless, the observation of a hypoxanthine burst ascertains that base release is faster than the steady-state turnover rate. Furthermore, this implies that the overall rate-determining step occurs after base release and is most likely ribose release.

Two-Step Ribose Binding. We studied the kinetics of the binding of ribose to the *Tbb* IG-NH using stopped-flow fluorescence. For this purpose, different amounts of ribose were mixed with a fixed amount of enzyme, yielding fluorescence transients that could be fit to a single exponential. The observed rate constants of these transients have a hyperbolic concentration dependency, consistent with a two-step binding mechanism. In the forward direction of the hydrolytic reaction, this slow unimolecular step converts the tightly bound enzyme·ribose complex into a loosely bound form from which ribose can easily dissociate. The rate of this unimolecular step is very comparable to the rate of product release determined from multiple turnovers of guanosine and 7mGuo (Table 3). On the basis of these data, we can conclude that this slow isomerization is the overall rate-limiting step on the reaction coordinate [$k_4 = 2.7$ s^{-1} (see Scheme 2)], supporting the interpretation that base release precedes ribose release. Hence, release of product from the *Tbb* IG-NH is strictly ordered, which was shown for the purine-specific *Tv* IAG-NH (*35*, *48*), and unlike what was observed for the *C. fasciculata* IU-NH (*8*).

Crystal Structure of the Tbb IG-NH. We determined the structure of the unliganded *Tbb* IG-NH using single-crystal X-ray diffraction to 2.5 Å (Table 4). The IG-NH subunit structure resembles the overall NH fold (*31*) with a parallel core β-sheet flanked by α-helices, and the catalytic site located in a cavity at the C-terminal end of the sheet (Figure 4). The structures of *Tbb* IG-NH and the *E. coli* RihB pyrimidine nucleosidase (*6*) superimpose with a root-mean-square deviation (rmsd) of 1.50 Å using 275 homologous Cα positions. Conversely, the *Tv*

Scheme 2: Minimal Kinetic Scheme for the Hydrolysis of 6-Oxopurine Nucleosides by the *Tbb* IG-NH

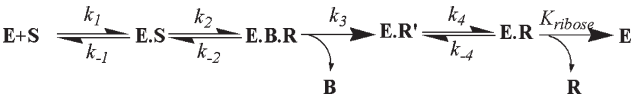

Table 4: Data Collection and Refinement Statistics

Data Collection	
cell parameters	a = 115.89 Å
	b = 124.48 Å
	c = 203.88 Å
	α = β = γ = 90°
space group	$C222_1$
wavelength (Å)	0.97565
resolution range (Å)	102.6−2.5 (2.6−2.5)
total no. of reflections ($I > -3\sigma$)	379095 (41211)
no. of unique reflections	51547 (5626)
completeness (%)	99.9 (99.6)
redundancy	7.4 (7.3)
$\langle I/\sigma(I)\rangle$	19.5 (5.5)
R_{sym}[a]	0.096 (0.502)
Wilson B factor (Å^2)	41.6
Refinement Statistics	
no. of reflections ($F > 0$)	48,812
R_{crys}[b]	0.189
R_{free}[c]	0.225
rmsd for bonds (Å)	0.014
rmsd for angles (deg)	1.439
residues in favored, allowed Ramachandran regions (%)	97.2, 99.7
atomic displacement parameter (Å^2)	
protein (chains A, B, C, D)	65.5, 65.9, 65.4, 65.3
solvent	45.0

[a]$R_{sym} = \sum_{hkl}\sum_i||I_i(hkl)| - |\langle I(hkl)\rangle||/\sum_{hkl}\sum_i I_i(hkl)$. [b]$R_{crys} = \sum_{hkl}||F_{obs}(hkl)| - |F_{calc}(hkl)||/\sum_{hkl}F_{obs}(hkl)$. [c]$R_{free}$ is the same as R_{crys} but was calculated using 2620 randomly selected reflections excluded from all stages of refinement.

IAG-NH (*15*) displays a rmsd of 1.43 Å over only 243 amino acids. Hence, the overall structure of the IG-NH subunit is more similar to that of CU- and IU-NHs than that of the functionally homologous IAG-NHs. The major structural differences between IG-NH and both IU- and IAG-NHs are the presence of two 3_{10} helices, η1 (spanning residues 146−150) and η2 (residues 290−292) and the insertion of helix α13 between strands β13 and β14. This element extends away from the catalytic site of the subunit to which the element belongs but is positioned in front of the opening of the active site of the neighboring subunit. Another insertion between helices α7 and α8 adopts an extended conformation and folds into a hairpin structure that resembles two short antiparallel β-strands. This region is, however, highly flexible and could only be traced in one IG-NH subunit. The crossover region of the core β-sheet, linking strands β3 and β4, is structurally homologous to the corresponding region in CU- and IU-NHs, with two random coil regions flanking a single α-helix rather than the two α-helical segments present in the *Tv* IAG-NH (Figure 2 of the Supporting Information).

Tetrameric Quaternary Structure of IG-NH. The recombinant *Tbb* IG-NH displays an apparent tetrameric quaternary structure in size exclusion chromatography and dynamic light scattering experiments (not shown), differing from the apparent homotrimer reported for the *Crithidia* IG-NH enzyme (*24*).

The *Tbb* IG-NH crystallized also as a homotetramer in the crystal asymmetric unit, with an internal 222 symmetry that closely resembles the tetrameric assembly of IU- and CU-NHs, being mediated by interactions between the same structural elements. Instead, the quaternary structure of *Tbb* IG-NH shares no resemblance with the dimeric *Tv* IAG-NH despite the strong similarity in substrate specificity and catalytic mechanism (Figure 4 and Figure 2 of the Supporting Information). The arrangement of the subunit is a dimer of dimers, with two distinct protein−protein interaction surfaces. The total protein surfaces buried at the interfaces are 988 and 1166 Å^2, which are significantly larger in comparison to the values of 891 and 1071 Å^2 for the RihB CU-NH or 851 and 754 Å^2 for the *Crithidia* IU-NH, respectively. The role of quaternary structure assembly in modulating NH function is still elusive. The active sites are entirely composed of residues from a single subunit, consistent with the lack of cooperativity observed in the kinetic analysis.

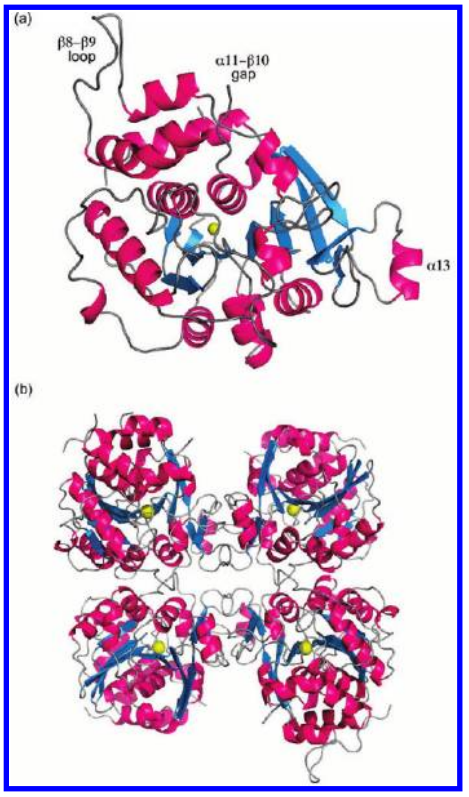

FIGURE 4: Structure of the *Tbb* IG-NH. (a) Overall structure of the *Tbb* IG-NH subunit, with α-helices depicted as pink ribbons, α-strands depicted as blue arrows, and loop regions colored gray. *Tbb* IG-NH maintains the overall NH fold and shares a higher degree of similarity with IU-NHs despite its functional similarity to IAG-NHs. (b) Structure of the *Tbb* IG-NH tetramer. The quaternary structure of *Tbb* IG-NH resembles the IU-NH tetramer, a dimer of dimers assembled using conserved structural elements.

A Highly Hydrophobic Base-Binding Subsite. The active site of the IG-NH is located in a deep cavity at the C-terminal end of the core β-sheet. The site can be subdivided into a hydrophilic bottom part, optimized for ribosyl binding and distortion, and an outer portion that interacts with the 6-oxopurine and stabilizes the negative charge that builds up in the base at the transition state of the hydrolysis reaction. The bottom of the cavity is lined by the side chain atoms of several hydrophilic residues (Figure 5), including residues Asp11, Asp16, and Asp280 and the main chain carbonyl oxygen of Leu131 involved in metal binding interactions. The active site Ca^{2+} is bound to the enzyme in a highly conserved octacoordination geometry, with three water molecules completing the ligation of the ion. All amino acid residues that are involved in ribosyl binding in other NHs are strictly conserved in the *Tbb* IG-NH, including Asn40, Glu177, and Asn179.

The outer portion of the catalytic cavity is remarkably hydrophobic in character, lined by the side chain atoms of Trp80, Phe83, Phe178, Trp205, and Pro279. The hydrophilic residues that have a potential for interactions with the purine base are Asp15, Asn40, and Asn171. In particular, Asn171 interacts via its side chain amide with the indole ring of Trp205 in a perpendicular geometry. This strong interaction suggests a fair amount of rigidity of these amino acids, and possibly a weak propensity for structural rearrangement upon binding of substrate. Although we were unsuccessful in crystallizing the *Tbb* IG-NH in complex with a competitive inhibitor, the similarities in the ribosyl binding site with other NHs make it fairly straightforward to model the substrate−enzyme interactions. A superposition of the different structures of ligand-bound IAG-NH, CU-NH, and IU-NH enzymes onto the IG-NH positions the ribosyl moiety of the substrates at the expected position, coordinating the Ca^{2+} ion. The orientation of the base with respect to the ribosyl moiety is instead forced by the characteristics of the catalytic cavity (Figure 6). The hypoxanthine base is forced by the walls of the

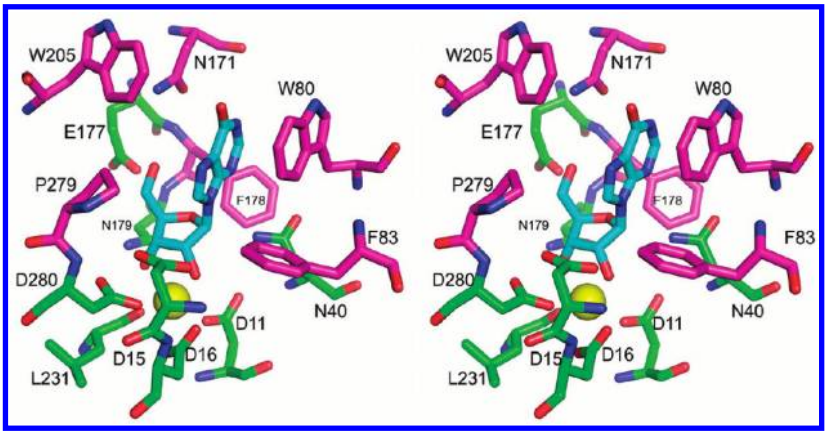

FIGURE 5: Stereoview of the active site of *Tbb* IG-NH. The active site residues involved in Ca^{2+} chelation and interactions with the ribose moiety in NHs are depicted with green carbon atoms. The residues potentially involved in interactions with the nitrogenous base are depicted with pink carbon atoms. A molecule of inosine was modeled by superposition of the structure of the *E. coli* CU-NH YeiK in complex with inosine without further intervention. Only residues within 4.5 Å of the inosine molecule are shown.

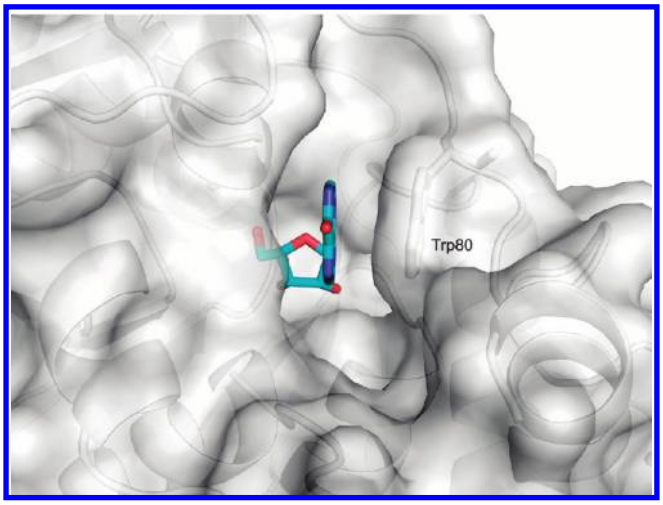

FIGURE 6: Molecular surface at the *Tbb* IG-NH active site. The molecular surface of the active site shows a tight fit of the hypoxanthine base (based on the model generated by superposition of the unliganded *Tbb* IG-NH structure with the YeiK−inosine complex structure) and a parallel $\pi-\pi$ interaction with residue Trp80.

active site in a conformation that is intermediate between the *syn* and *anti* configurations. Interestingly, the conformation closely matches that observed in the CU-NH in complex with inosine (*49*) but drastically differs from what was determined for the *Tv* IAG-NH (*27*). In this conformation, inosine can interact with Trp80 via stacking interactions and is also positioned in close van der Waals contact with the side chains of Phe83, Phe178, Trp205, and Pro279. This orientation also allows the face-to-face interaction with the side chain amide of Asn171, and possible hydrogen bonds with Asn40 (Figure 5). Further interactions could likely be provided by amino acids 256−273 from the flexible loop linking helix α11 to strand β10, disordered in the structure presented here, that includes four Asp residues, one His, and one Arg. Moreover, helix α13 also points the hydrophilic side chains of Thr321, Gln323, Ser324, and Lys327 toward the active site and could mediate interactions with the substrate via a swinging movement.

DISCUSSION

Lacking the enzymatic activities required for purine base biosynthesis, trypanosomes have evolved efficient scavenging systems (*4*). The NH-dependent scavenging pathway is characterized by three distinct NH isozymes with different substrate specificities and kinetic properties. Here we report the first full molecular, functional, and structural characterization of the yet uncharacterized isozyme, the 6-oxopurine-specific IG-NH from *T. brucei brucei*.

The steady-state kinetic analysis of *Tbb* IG-NH (Table 1) shows that the highest activity is found for inosine and guanosine exemplary for an IG-specific NH, although the IG specificity is less pronounced compared to that of the enzyme from *C. fasciculata* (*24*). The enzyme is very efficient with specificity constants (k_{cat}/K_M) for inosine and guanosine almost equal to the rate expected for a diffusion-limited reaction. Both the IG-NHs and the IAG-NHs are thus very efficient enzymes for purine hydrolysis (*25*, *26*), underscoring their crucial role in purine catabolism in trypanosomes. Indeed, their catalytic efficiencies are at least 1 order of magnitude greater than those of the nonspecific isozymes from other flagellates (*14*, *15*), or even pyrimidine-specific NHs from bacteria and yeast (*49*). Moreover, the K_M values for purine nucleosides are in the low micromolar range for IG- and IAG-NHs, while in IU- and CU-NHs, they approach the millimolar values. The low K_M values exhibited by both IG- and IAG-NHs are likely to facilitate the capture of substrates in the trypanosome. Because the concentration of inosine in human plasma is estimated to be 1 μM (*24*), it is obvious that IG- and IAG-NHs play the central role in rescuing nucleosides from the host for the synthesis of RNA, DNA, and cofactors. In fact, a recent study showed that a nanomolar inhibitor of the *Tbb* IAG-NH is effective in killing trypanosomes in a murine model of infection (*11*). The IAG-NH from *Tbb* has lower k_{cat} values and higher K_M values than the *Tbb* IG-NH analyzed here, suggesting that the latter is the main NH in *Tbb* for inosine and guanosine processing, while the IAG-NH probably focuses on adenosine hydrolysis (*25*).

The *Tbb* IG-NH's activity profile clearly shows that the exocyclic group at position 6 of the purine base ring plays a crucial role in catalysis. A functional group with H-acceptor capabilities at position 6 leads to a high rate of turnover of purine substrates, demonstrated by the kinetic parameters of inosine, guanosine, ethenoadenosine, and xanthosine. In contrast, a lower turnover rate and a higher affinity are observed when the purine ring contains a functional group with H-donor capacities linked to the C6 atom, as in purine riboside, 2-aminopurine ribose, and adenosine.

The IG-NH is like the IAG-NHs, truly purine-specific (see Table 1), with k_{cat}/K_M ratios 1000−1000000 times higher for the naturally occurring purine nucleosides then for the pyrimidine nucleosides (Table 1), yet the only requirement for efficient catalysis seems to be the presence of the purine ring, because the hydrolysis of purine riboside, which lacks all exocyclic groups on the purine ring, is as effectively catalyzed as that of the other purine nucleosides. Adenosine displays a submicromolar K_M coupled to a k_{cat} 2 orders of magnitude lower than the k_{cat} for 6-oxopurine nucleosides (0.24 s^{-1}). This finding suggests that the substrate specificity of *Tbb* IG-NH is determined by catalytic turnover rather than specific binding interactions and takes advantage of the presence of the carbonyl group at C6 of the purine ring to lower the transition-state barrier. This could be effectively achieved by stabilizing the partial negative charge developing in the purine ring through resonance forms delocalizing the negative charge to the C6 carbonyl. The same delocalization is not as favorable for the adenine base, because the negatively charged amine is energetically less favored. Similar events have been proposed to play a role in the catalytic mechanism of bacterial purine nucleoside phosphorylases (*50*).

Tbb IG-NH is the only so far characterized NH that is able to catalyze the hydrolysis of 3-deazaadenosine, indicating that N3 of the purine ring is less important for catalysis than for NHs from other specificity classes. The low K_M for 3-deazaadenosine moreover shows that the purine N3 atom is not involved in any binding interactions. The substrate analogue *p*-nitrophenyl β-D-ribofuranoside (pNPR) does not require protonation at the leaving group but is susceptible to O-glycosidic bond hydrolysis when the ribosyl moiety is converted to the oxocarbenium ion. pNPR is a relatively poor substrate for the *Tbb* IG-NH, hence indicating that the enzyme attains a considerable fraction of its catalytic power via leaving group activation rather than via ribosyl distortion. Nevertheless, the kinetic constants of the deoxynucleosides (Table 1) highlight the critical importance in

catalysis of all three hydroxyl groups of the ribose moiety of the substrate.

On the basis of the pre-steady-state analysis, we can suggest a minimal kinetic scheme (Scheme 2) for the hydrolysis of 6-oxopurine nucleosides by *Tbb* IG-NH and determine all rate constants involved in this reaction scheme (Table 3). This scheme is based on a reversible chemistry step followed by an ordered product release with base release preceding ribose release. Base release (k_3, Scheme 2 and Table 3) is followed by a slow isomerization (k_4 and k_{-4} in Scheme 2 and Table 3) from a tightly bound (E·R′) to a loosely bound (E·R) enzyme·ribose complex prior to ribose dissociation. This isomerization is the overall rate-determining step of the hydrolytic reaction.

The finding that this slow step prior to ribose dissociation (2.7 s^{-1} at 5 °C, k_4 in Scheme 2 and Table 1), which should be independent of the substrate used, is faster than the catalytic turnover of adenosine (0.24 s^{-1} at 35 °C, k_{cat} in Table 1) could suggest that the rate-limiting step for adenosine hydrolysis catalyzed by *Tbb* IG-NH is shifted from product release to a very slow inefficient chemistry step. Therefore, the overall catalytic turnover rate will probably be determined by chemistry for adenosine hydrolysis, while the catalytic turnover rate of 6-oxopurine nucleoside hydrolysis is determined by ribose release. This shift in rate-limiting step between 6-oxopurine nucleosides and other purine nucleosides points to an even greater degree of discrimination between adenosine and 6-oxopurine nucleosides on the chemistry level as suggested by the steady-state k_{cat} and further corroborates our statement above that the substrate specificity is determined by the catalytic (chemistry) step.

Here we demonstrate that the chemistry step of the hydrolysis of guanosine and 7mGuo catalyzed by *Tbb* IG-NH is reversible. No reversibility of the chemistry step was discovered for purine hydrolysis by the *Tv* IAG-NH (*35*). Moreover, a higher reversibility of the chemistry step is observed for guanosine than for 7mGuo hydrolysis catalyzed by *Tbb* IG-NH (Table 2). 7mGuo is a guanosine analogue with an activated (positively charged) purine ring that needs no further leaving group activation by enzymatic protonation (*51*). Thus, the observed difference in the on-enzyme reversibility could be explained on the basis of the lower nucleophilicity of the 7-methylguanine base toward ribose compared to guanine. The reason for the difference between the on-enzyme reversibility of guanosine hydrolysis catalyzed by *Tv* IAG-NH and *Tbb* IG-NH remains to be clarified.

Overall, this pre steady-state kinetic analysis of the *Tbb* IG-NH demonstrates that the IAG- and IG-specific nucleoside hydrolases have very comparable kinetic mechanisms (*35*). In both mechanisms, the isomerization necessary to convert a tightly bound enzyme·ribose complex to a loosely bound complex prior to ribose dissociation is the overall rate-determining step. Hence, it is very tempting to suggest that this mechanism is generally applicable for the nucleoside hydrolase family, or at least for the purine-specific NHs. The two flexible loops named loop I and II are common features of members of the NH family. For all specificity classes, two distinct conformations of these loops have been observed: an open ligand free form and a closed ligand-bound state (*29*, *30*). For the *Tv* IAG-NH, it was shown that flexible loop II (corresponding to flexible residues 256−273 in *Tbb* IG-NH) is involved in the overall rate-determining isomerization prior to ribose dissociation (*52*). This region shows very high flexibility in the determined crystal structure of *Tbb* IG-NH, and the same slow isomerization prior to ribose dissociation is observed. Therefore, it is likely that this loop restructuring is involved in ribose release and determines the steady-state turnover rates of this *Tbb* IG-NH, perhaps even of all NHs. This hypothesis further implies that the flexible loop II could be a conserved functional element in the catalytic mechanism of the nucleoside hydrolase family.

The *Tbb* IG-NH structure represents yet another variation from the standard NH fold (*26*, *31*). Despite its functional and mechanistic similarities to IAG-NHs, the IG-NH displays more tertiary and quaternary structure similarity to IU- and CU-NHs (Figure 2 of the Supporting Information). However, while the *Tbb* IG-NH maintains the trademark Ca^{2+}-containing active site for ribosyl binding and discrimination, the region devoted to base interaction displays unique features compared to the other specificity classes. The walls of the active site cavity of NHs are devoted to binding interactions with the substrate nitrogenous base, and its stabilization along the reaction coordinate (*27*, *28*, *49*). A conserved histidine residue, whose mutation to alanine reduces the catalytic efficiency of the *Cf* IU-NH by a factor of 3800, making it likely to act as a general acid (*7*), is a trademark of IU-NHs. The *Tbb* IG-NH lacks this histidine residue, thus reflecting the closer functional similarity with IAG-NH. However, this is achieved in the context of a different structural framework (Figure 3 of the Supporting Information). The model of inosine bound to the IG-NH active site clearly suggests an important role of aromatic stacking mediated by residue Trp80 in the catalytic mechanism, similar to the pK_a-increasing stacking proposed for the *Tv* IAG-NH (*27*). In contrast to IAG-NH, the conformation of the docked inosine (intermediate between *syn* and *anti*) does not allow a O5′−HC8 hydrogen bond to further stabilize the negative charge developing in the purine ring at the transition state (Figure 6 and Figure 3 of the Supporting Information). Hence, hydrophilic or charged residues, the ones present in the flexible loop II linking helix α11 to strand β10 in the *Tbb* IG-NH, are likely to participate in the leaving group activation and/or stabilization via specific interactions. Moreover, helix α13, which in the unliganded IG-NH structure is more than 7 Å from the active site, could perhaps relocate upon substrate binding. The residues in this helix are conserved in all closely related, trypanosomal IG-NH homologues, supporting a possible role in enzymatic function.

The molecular characterization of protozoal NHs has long been considered as an attractive approach for the development of selective, potent antitrypanosomal compounds. Immucillins were among the first nanomolar NH inhibitors identified and are effective against IU-, IAG-, and IG-NHs. These compounds have proven to be effective in killing *Plasmodium falciparum* in human erythrocytes (*53*), a pathogenic protozoan that causes malaria and is also purine-auxotrophic, though it relies for base salvage on purine nucleoside phosphorylase and not NHs. Moreover, Immucillins are approved for use against T cell lymphomas as PNP inhibitors (*54*). The availability of detailed kinetic and structural information for all specificity classes of the trypanosomal NHs now provides a formidable template for specific targeting of the protozoal nucleobase salvage pathway. Indeed, N-arylmethyl-substituted iminoribitols are selective, potent inhibitors of purine-specific NHs (*55*) and have proven to be effective in trypansomal infection models (*11*). Further development of these compounds will take advantage of the fine understanding of the NH structure and enzymatic properties.

ACKNOWLEDGMENT

We acknowledge the use of beamline ID14-EH4 at the European Synchrotron Radiation Facility.

SUPPORTING INFORMATION AVAILABLE

Sample electron density map, structural comparison of tertiary structures of NHs from different specificity classes, and active site comparison between *Tbb* IG-NH and *Tv* IAG-NH. This material is available free of charge via the Internet at http://pubs.acs.org.

REFERENCES

1. Barrett, M. P., Burchmore, R. J., Stich, A., Lazzari, J. O., Frasch, A. C., Cazzulo, J. J., and Krishna, S. (2003) The trypanosomiases. *Lancet 362*, 1469–1480.
2. Markell, E. K., John, D. T., and Krotoski, W. A. (1999) Markell and Voge's Medical Prasitology, 8th ed., W. B. Saunders Co., Philadelphia.
3. Naula, C., and Burchmore, R. (2003) A plethora of targets, a paucity of drugs: Progress towards the development of novel chemotherapies for human African trypanosomiasis. *Expert Rev. Anti-Infect. Ther. 1*, 157–165.
4. Berriman, M., Ghedin, E., Hertz-Fowler, C., Blandin, G., Renauld, H., Bartholomeu, D. C., Lennard, N. J., Caler, E., Hamlin, N. E., Haas, B., Bohme, U., Hannick, L., Aslett, M. A., Shallom, J., Marcello, L., Hou, L., Wickstead, B., Alsmark, U. C., Arrowsmith, C., Atkin, R. J., Barron, A. J., Bringaud, F., Brooks, K., Carrington, M., Cherevach, I., Chillingworth, T. J., Churcher, C., Clark, L. N., Corton, C. H., Cronin, A., Davies, R. M., Doggett, J., Djikeng, A., Feldblyum, T., Field, M. C., Fraser, A., Goodhead, I., Hance, Z., Harper, D., Harris, B. R., Hauser, H., Hostetler, J., Ivens, A., Jagels, K., Johnson, D., Johnson, J., Jones, K., Kerhornou, A. X., Koo, H., Larke, N., Landfear, S., Larkin, C., Leech, V., Line, A., Lord, A., Macleod, A., Mooney, P. J., Moule, S., Martin, D. M., Morgan, G. W., Mungall, K., Norbertczak, H., Ormond, D., Pai, G., Peacock, C. S., Peterson, J., Quail, M. A., Rabbinowitsch, E., Rajandream, M. A., Reitter, C., Salzberg, S. L., Sanders, M., Schobel, S., Sharp, S., Simmonds, M., Simpson, A. J., Tallon, L., Turner, C. M., Tait, A., Tivey, A. R., Van Aken, S., Walker, D., Wanless, D., Wang, S., White, B., White, O., Whitehead, S., Woodward, J., Wortman, J., Adams, M. D., Embley, T. M., Gull, K., Ullu, E., Barry, J. D., Fairlamb, A. H., Opperdoes, F., Barrell, B. G., Donelson, J. E., Hall, N., Fraser, C. M., Melville, S. E., and El-Sayed, N. M. (2005) The genome of the African trypanosome *Trypanosoma brucei*. *Science 309*, 416–422.
5. Hammond, D. J., and Gutteridge, W. E. (1984) Purine and pyrimidine metabolism in the Trypanosomatidae. *Mol. Biochem. Parasitol. 13*, 243–261.
6. Giabbai, B., and Degano, M. (2004) Crystal structure to 1.7 Å of the *Escherichia coli* pyrimidine nucleoside hydrolase YeiK, a novel candidate for cancer gene therapy. *Structure 12*, 739–749.
7. Gopaul, D. N., Meyer, S. L., Degano, M., Sacchettini, J. C., and Schramm, V. L. (1996) Inosine-uridine nucleoside hydrolase from *Crithidia fasciculata*. Genetic characterization, crystallization, and identification of histidine 241 as a catalytic site residue. *Biochemistry 35*, 5963–5970.
8. Parkin, D. W., Horenstein, B. A., Abdulah, D. R., Estupinan, B., and Schramm, V. L. (1991) Nucleoside hydrolase from *Crithidia fasciculata*. Metabolic role, purification, specificity, and kinetic mechanism. *J. Biol. Chem. 266*, 20658–20665.
9. Berg, M., Bal, G., Goeminne, A., Van der Veken, P., Versees, W., Steyaert, J., Haemers, A., and Augustyns, K. (2009) Synthesis of bicyclic N-arylmethyl-substituted iminoribitol derivatives as selective nucleoside hydrolase inhibitors. *ChemMedChem 4*, 249–260.
10. Miles, R. W., Tyler, P. C., Evans, G. B., Furneaux, R. H., Parkin, D. W., and Schramm, V. L. (1999) Iminoribitol transition state analogue inhibitors of protozoan nucleoside hydrolases. *Biochemistry 38*, 13147–13154.
11. Berg, M., Kohl, L., Van der Veken, P., Joossens, J., Al-Salabi, M. I., Castagna, V., Giannese, F., Cos, P., Versees, W., Steyaert, J., Grellier, P., Haemers, A., Degano, M., Maes, L., de Koning, H. P., and Augustyns, K. (2010) Evaluation of nucleoside hydrolase inhibitors for treatment of African trypanosomiasis. *Antimicrob. Agents Chemother. 54*, 1900–1908.
12. Miller, R. L., Sabourin, C. L., Krenitsky, T. A., Berens, R. L., and Marr, J. J. (1984) Nucleoside hydrolases from *Trypanosoma cruzi*. *J. Biol. Chem. 259*, 5073–5077.
13. Pelle, R., Schramm, V. L., and Parkin, D. W. (1998) Molecular cloning and expression of a purine-specific N-ribohydrolase from *Trypanosoma brucei brucei*. Sequence, expression, and molecular analysis. *J. Biol. Chem. 273*, 2118–2126.
14. Shi, W., Schramm, V. L., and Almo, S. C. (1999) Nucleoside hydrolase from *Leishmania major*. Cloning, expression, catalytic properties, transition state inhibitors, and the 2.5-Å crystal structure. *J. Biol. Chem. 274*, 21114–21120.
15. Versees, W., Decanniere, K., Pelle, R., Depoorter, J., Brosens, E., Parkin, D. W., and Steyaert, J. (2001) Structure and function of a novel purine specific nucleoside hydrolase from *Trypanosoma vivax*. *J. Mol. Biol. 307*, 1363–1379.
16. Petersen, C., and Moller, L. B. (2001) The RihA, RihB, and RihC ribonucleoside hydrolases of *Escherichia coli*. Substrate specificity, gene expression, and regulation. *J. Biol. Chem. 276*, 884–894.
17. Hunt, C., Gillani, N., Farone, A., Rezaei, M., and Kline, P. C. (2005) Kinetic isotope effects of nucleoside hydrolase from *Escherichia coli*. *Biochim. Biophys. Acta 1751*, 140–149.
18. Ogawa, J., Takeda, S., Xie, S. X., Hatanaka, H., Ashikari, T., Amachi, T., and Shimizu, S. (2001) Purification, characterization, and gene cloning of purine nucleosidase from *Ochrobactrum anthropi*. *Appl. Environ. Microbiol. 67*, 1783–1787.
19. Versees, W., Van Holsbeke, E., De Vos, S., Decanniere, K., Zegers, I., and Steyaert, J. (2003) Cloning, preliminary characterization and crystallization of nucleoside hydrolases from *Caenorhabditis elegans* and *Campylobacter jejuni*. *Acta Crystallogr. D59*, 1087–1089.
20. Kurtz, J. E., Exinger, F., Erbs, P., and Jund, R. (2002) The URH1 uridine ribohydrolase of *Saccharomyces cerevisiae*. *Curr. Genet. 41*, 132–141.
21. Ribeiro, J. M., and Valenzuela, J. G. (2003) The salivary purine nucleosidase of the mosquito *Aedes aegypti*. *Insect Biochem. Mol. Biol. 33*, 13–22.
22. Porcelli, M., Concilio, L., Peluso, I., Marabotti, A., Facchiano, A., and Cacciapuoti, G. (2008) Pyrimidine-specific ribonucleoside hydrolase from the archaeon *Sulfolobus solfataricus*: Biochemical characterization and homology modeling. *FEBS J. 275*, 1900–1914.
23. Porcelli, M., Peluso, I., Marabotti, A., Facchiano, A., and Cacciapuoti, G. (2009) Biochemical characterization and homology modeling of a purine-specific ribonucleoside hydrolase from the archaeon *Sulfolobus solfataricus*: Insights into mechanisms of protein stabilization. *Arch. Biochem. Biophys. 483*, 55–65.
24. Estupinan, B., and Schramm, V. L. (1994) Guanosine-inosine-preferring nucleoside N-glycohydrolase from *Crithidia fasciculata*. *J. Biol. Chem. 269*, 23068–23073.
25. Parkin, D. W. (1996) Purine-specific nucleoside N-ribohydrolase from *Trypanosoma brucei brucei*. Purification, specificity, and kinetic mechanism. *J. Biol. Chem. 271*, 21713–21719.
26. Versees, W., and Steyaert, J. (2003) Catalysis by nucleoside hydrolases. *Curr. Opin. Struct. Biol. 13*, 731–738.
27. Versees, W., Decanniere, K., Van Holsbeke, E., Devroede, N., and Steyaert, J. (2002) Enzyme-substrate interactions in the purine-specific nucleoside hydrolase from *Trypanosoma vivax*. *J. Biol. Chem. 277*, 15938–15946.
28. Degano, M., Almo, S. C., Sacchettini, J. C., and Schramm, V. L. (1998) Trypanosomal nucleoside hydrolase. A novel mechanism from the structure with a transition-state inhibitor. *Biochemistry 37*, 6277–6285.
29. Versees, W., Barlow, J., and Steyaert, J. (2006) Transition-state complex of the purine-specific nucleoside hydrolase of *T. vivax*: Enzyme conformational changes and implications for catalysis. *J. Mol. Biol. 359*, 331–346.
30. Versees, W., Goeminne, A., Berg, M., Vandemeulebroucke, A., Haemers, A., Augustyns, K., and Steyaert, J. (2009) Crystal structures of *T. vivax* nucleoside hydrolase in complex with new potent and specific inhibitors. *Biochim. Biophys. Acta 1794*, 953–960.
31. Degano, M., Gopaul, D. N., Scapin, G., Schramm, V. L., and Sacchettini, J. C. (1996) Three-dimensional structure of the inosine-uridine nucleoside N-ribohydrolase from *Crithidia fasciculata*. *Biochemistry 35*, 5971–5981.
32. Thompson, J. D., Higgins, D. G., and Gibson, T. J. (1994) CLUSTAL W: Improving the sensitivity of progressive multiple sequence alignment through sequence weighting, position-specific gap penalties and weight matrix choice. *Nucleic Acids Res. 22*, 4673–4680.
33. Pace, C. N., Vajdos, F., Fee, L., Grimsley, G., and Gray, T. (1995) How to measure and predict the molar absorption coefficient of a protein. *Protein Sci. 4*, 2411–2423.
34. Cook, P. F., and Cleland, W. W. (2007) Initial velocity studies: Presence of added inhibitors. In Enzyme Kinetics and Mechanism (Shank, D., Rogers, R. L., and Scholl, S., Eds.) p 121, Taylor and Francis Group, New York.

35. Vandemeulebroucke, A., Versees, W., Steyaert, J., and Barlow, J. N. (2006) Multiple transients in the pre-steady-state of nucleoside hydrolase reveal complex substrate binding, product base release, and two apparent rates of chemistry. *Biochemistry 45*, 9307–9318.
36. Kabsch, W. (1988) Automatic indexing of rotation diffraction patterns. *J. Appl. Crystallogr. 21*, 67–72.
37. French, G. S., and Wilson, K. S. (1978) On the treatment of negative intensity observations. *Acta Crystallogr. A34*, 517–525.
38. Vagin, A. A., and Isupov, M. N. (2001) Spherically averaged phased translation function and its application to the search for molecules and fragments in electron-density maps. *Acta Crystallogr. D57*, 1451–1456.
39. Cowtan, K. (1994) *Joint CCP4 and ESF-EACBM Newsletter on Protein Crystallography 31*, 34–38.
40. Jones, T. A., Zou, J., Cowan, S. W., and Kjeldgaard, M. (1991) Improved methods for building protein models in electron density maps and the location of errors in these models. *Acta Crystallogr. A47*, 110–119.
41. Murshudov, G. N., Vagin, A. A., and Dodson, E. J. (1997) Refinement of macromolecular structures by the maximum-likelihood method. *Acta Crystallogr. D53*, 240–255.
42. Winn, M. D., Isupov, M. N., and Murshudov, G. N. (2001) Use of TLS parameters to model anisotropic displacements in macromolecular refinement. *Acta Crystallogr. D57*, 122–133.
43. Davis, I. W., Murray, L. W., Richardson, J. S., and Richardson, D. C. (2004) MOLPROBITY: Structure validation and all-atom contact analysis for nucleic acids and their complexes. *Nucleic Acids Res. 32*, W615–W619.
44. Morris, R. J., Perrakis, A., and Lamzin, V. S. (2003) ARP/wARP and automatic interpretation of protein electron density maps. *Methods Enzymol. 374*, 229–244.
45. Goeminne, A., McNaughton, M., Bal, G., Surpateanu, G., Van der Veken, P., De Prol, S., Versees, W., Steyaert, J., Apers, S., Haemers, A., and Augustyns, K. (2007) 1,2,3-Triazolylalkylribitol derivatives as nucleoside hydrolase inhibitors. *Bioorg. Med. Chem. Lett. 17*, 2523–2526.
46. Goeminne, A., McNaughton, M., Bal, G., Surpateanu, G., Van Der Veken, P., De Prol, S., Versees, W., Steyaert, J., Haemers, A., and Augustyns, K. (2008) Synthesis and biochemical evaluation of guanidino-alkyl-ribitol derivatives as nucleoside hydrolase inhibitors. *Eur. J. Med. Chem. 43*, 315–326.
47. Vandemeulebroucke, A., Versees, W., De Vos, S., Van Holsbeke, E., and Steyaert, J. (2003) Pre-steady-state analysis of the nucleoside hydrolase of *Trypanosoma vivax*. Evidence for half-of-the-sites reactivity and rate-limiting product release. *Biochemistry 42*, 12902–12908.
48. Barlow, J. N., and Steyaert, J. (2007) Examination of the mechanism and energetic contribution of leaving group activation in the purine-specific nucleoside hydrolase from *Trypanosoma vivax*. *Biochim. Biophys. Acta 1774*, 1451–1461.
49. Iovane, E., Giabbai, B., Muzzolini, L., Matafora, V., Fornili, A., Minici, C., Giannese, F., and Degano, M. (2008) Structural basis for substrate specificity in group I nucleoside hydrolases. *Biochemistry 47*, 4418–4426.
50. Deng, H., Cahill, S. M., Abad, J. L., Lewandowicz, A., Callender, R. H., Schramm, V. L., and Jones, R. A. (2004) Active site contacts in the purine nucleoside phosphorylase−hypoxanthine complex by NMR and ab initio calculations. *Biochemistry 43*, 15966–15974.
51. Versees, W., Loverix, S., Vandemeulebroucke, A., Geerlings, P., and Steyaert, J. (2004) Leaving group activation by aromatic stacking: An alternative to general acid catalysis. *J. Mol. Biol. 338*, 1–6.
52. Vandemeulebroucke, A., De Vos, S., Van Holsbeke, E., Steyaert, J., and Versees, W. (2008) A flexible loop as a functional element in the catalytic mechanism of nucleoside hydrolase from *Trypanosoma vivax*. *J. Biol. Chem. 283*, 22272–22282.
53. Kicska, G. A., Tyler, P. C., Evans, G. B., Furneaux, R. H., Schramm, V. L., and Kim, K. (2002) Purine-less death in *Plasmodium falciparum* induced by immucillin-H, a transition state analogue of purine nucleoside phosphorylase. *J. Biol. Chem. 277*, 3226–3231.
54. Schramm, V. L. (2004) Immucillins as antibiotics for T-cell proliferation and malaria. *Nucleosides, Nucleotides Nucleic Acids 23*, 1305–1311.
55. Goeminne, A., Berg, M., McNaughton, M., Bal, G., Surpateanu, G., Van der Veken, P., De Prol, S., Versees, W., Steyaert, J., Haemers, A., and Augustyns, K. (2008) N-Arylmethyl substituted iminoribitol derivatives as inhibitors of a purine specific nucleoside hydrolase. *Bioorg. Med. Chem. 16*, 6752–6763.